Magnetoelastic coupling within a Landau model of phase transitions: Application to the frustrated triangular antiferromagnet $CsNiCl_3$

G. Quirion,* X. Han, and M. L. Plumer

Department of Physics and Physical Oceanography, Memorial University, St. John's, Newfoundland A1B 3X7, Canada

(Received 11 January 2011; revised manuscript received 20 May 2011; published 21 July 2011)

A model Landau free energy is proposed in order to describe elastic coupling to spin degrees of freedom in systems exhibiting phase transitions which involve long-range magnetic order. Using rigourous symmetry arguments, various interaction terms are derived for magnetic materials with a hexagonal crystal structure. The model is applied to the frustrated triangular antiferromagnet $CsNiCl_3$ and used to analyze and correlate a wide variety of experimental results such as the magnetic phase diagram, magnetization, strains, and elastic constant measurements at low temperatures. Good agreement between the model and the data is obtained for the temperature and magnetic field dependence of C_{33} and C_{66} in the vicinity of phase transitions. In particular, the analysis shows that the anomaly observed in the field dependence of C_{33}, close to the spin-flop phase boundary ($H_{SF} \simeq 2$ T), is dominated by the field dependence of the magnetic susceptibility. It is also found that higher order magnetoelastic coupling terms are required to reproduce the qualitative behavior of the elastic constants in the vicinity of the phase transitions. Our results demonstrate that a straightforward mean-field model which incorporates the correct system symmetries provides a powerful tool for relating complex spin configurations to the elastic and other response functions. The present work also serves to complement and expand our earlier results [G. Quirion *et al.*, Phys. Rev. Lett. **97**, 077202 (2006)].

DOI: 10.1103/PhysRevB.84.014408 PACS number(s): 75.10.−b, 75.30.Kz, 75.40.Cx, 62.20.de

I. INTRODUCTION

Over the past several decades, interest in triangular antiferromagnetic systems has remained substantial due to the fact that spin frustration is known to lead to exotic magnetic properties giving rise to new classes of phase transitions as well as magnetoelectric phenomena.[1,2] The interplay among geometrical exchange frustration, anisotropy, thermal fluctuations, and an applied magnetic field (H) in these systems can yield to a wide variety of unusual types of magnetic (H-T) phase diagrams.[3,4] In many cases, these exhibit novel multicritical points which can reveal information on the critical behavior. Detailed understanding of the spin structures involved in this class of materials has been achieved through analyses of Landau-type free energies which are based on rigorous symmetry arguments. This has led to very good quantitative agreement between the phenomenological Landau approach and experimental data for H-T phase diagrams.[5,6] Free energy expansions which are based on a molecular field treatment of the spin Hamiltonian can reproduce only qualitative features of the phase diagrams. Monte Carlo simulations based on the same spin Hamiltonian have been somewhat more successful.[4,7]

Magnetoelastic coupling and its effects on ultrasonic velocity and the elastic constants, C_{ij}, has proven to be useful for the study of magnetic phase diagrams in the triangular antiferromagnet.[8–10] This is partly due to the fact that crystal symmetry plays a significant role in these measurements as well as in the spin structures themselves. The principal utility of such experimental results is to map out phase diagrams based on anomalous features in the elastic response functions indicating the location of a magnetic transition. More detailed measurements, along with analysis based on linear response theory, reveals relationships between the elastic constants and the order parameters which allows for the determination of critical behavior.[9] Analysis based on a Landau free energy expanded to low order typically shows a discontinuity in the C_{ij} at a continuous phase transition. As shown in the present work, the inclusion of higher order effects can be used to reveal more information on the temperature and field dependence of the C_{ij} in the vicinity of the transition.

Particular interest in antiferromagnetic compounds with triangular symmetry was triggered by the observation of a 120° magnetic order which, according to Kawamura,[11] should belong to new chiral universality classes. For that reason, these systems have been closely examined using renormalization-group techniques, Monte Carlo simulations, and experimentally.[1,11–15] While many of these works seem to support Kawamura's prediction, recent ultrasonic sound velocity measurements[16] on $CsNiCl_3$ reveal clear evidence that the 120° phase transition is rather weakly first order. This observation is consistent with other theoretical and numerical studies[7,17–22] and new Monte Carlo simulations on the XY stacked triangular antiferromagnet.[23]

The analysis of elastic properties of $CsNiCl_3$, presented in Ref. 16, played a crucial role in identifying the true nature of the magnetic phase transitions observed in $CsNiCl_3$. Based on a Landau-type free energy, the predicted scaling relations between the order parameters and the elastic constants were used to support conclusions made regarding the critical behavior. In particular, the model shows how the temperature dependence of the elastic constant C_{66} can be used to determine the value of critical exponent β. From this analysis, it was established that the exponent β is clearly field dependent in the 120° phase, demonstrating that the 120° phase transition in $CsNiCl_3$ does not belong to a new universality.[11]

We present here a full derivation of the Landau model used in Ref. 16. Furthermore, in order to validate our model, the numerical predictions are compared to the measured phase diagram, magnetization, strains, and elastic constants.

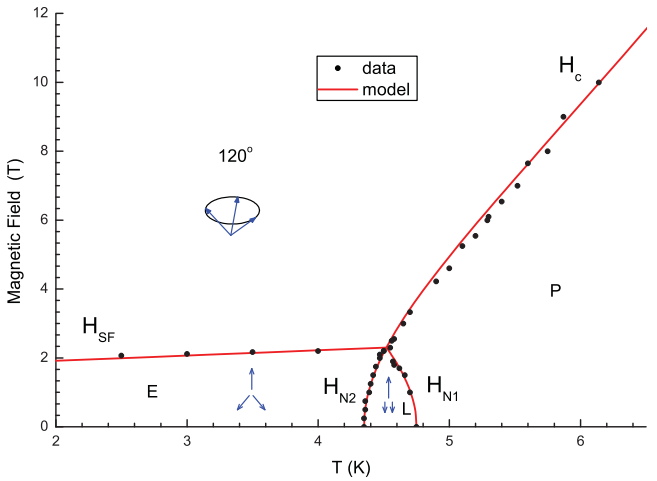

FIG. 1. (Color online) Magnetic phase diagram of $CsNiCl_3$ for $\mathbf{H}\|\hat{\mathbf{c}}$. Solid (red) lines represent the phase boundaries (H_{N_1},H_{N_2}, H_c, H_{SF}) based on the free energy, Eq. (10) (see Appendix).[5] Experimental data were obtained from anomalies observed on sound velocity measurements as a function of temperature or magnetic field (this work). Labels P, L, E, and 120° represent the paramagnetic, linear, elliptical, and 120° phases, respectively.

A member of numerous magnetic ABX_3 compounds,[1] $CsNiCl_3$ possesses a strong c-axis antiferromagnetic exchange with easy axis anisotropy. With an external field applied along the c axis, the competing interactions lead to the phase diagram shown in Fig. 1. At zero field, the c-axis anisotropy gives rise to a linear (L) ordered state at $T_{N_1} = 4.75$ K. With further cooling, an additional in-plane ordering set in at $T_{N_2} = 4.38$ K, resulting in an elliptical (E) spin polarization. A discussion of the critical exponent β associated with these two zero-field transitions is given in Ref. 16. Due to the easy axis anisotropy, an applied field along the c axis induces a spin-flop phase transition at $H_{SF} \sim 2$ T. In this new phase, the spins adopt the 120° spin structure commonly observed in frustrated triangular antiferromagnets. The transition boundary (H_c) between the 120° and the paramagnetic (P) phases thus belongs to the speculated chiral "universality" class. These three phases meet at an unusual type of multicritical point at ($T_m = 4.52$ K, $H_m = 2.30$ T).[5]

In addition to its unusual phase diagram associated with long-range magnetic order, $CsNiCl_3$ has also been much studied as a good example of a one-dimensional spin-1 Haldane antiferromagnet.[24] Of possible relevance to the present work is evidence for the effects of short-range fluctuations associated with this exotic quantum state on magnetization measurements in the paramagnetic state.[25,26] The present study is based on classical symmetry arguments and is purely phenomenological. Numerical estimation of model coefficients by comparison with experimental data makes no reference to possible microscopic origins of the interactions but may well reflect some fluctuations effects to the extent that they are captured by classical symmetry theory. Our work concerns the interplay between classical long-range magnetic order and the elastic properties of triangular antiferromagnets, in general, and $CsNiCl_3$, in particular.

The principal focus of this paper is on a comparison of experimental data and Landau-model results for the magnetic and elastic properties of $CsNiCl_3$ and how various thermodynamic linear response functions are related near the wide variety of phase transitions. We briefly describe the experimental methods in Sec. II, while details regarding the derivation of the Landau model, which takes into account the magnetoelastic couplings, are given in Sec. III. Sections IV and V are devoted to the analysis of the magnetic and elastic properties of $CsNiCl_3$. Finally, further comments and conclusion are made in Sec. VI. Details regarding how the model's coefficients are determined from the magnetic phase diagram, magnetization, strain, and elastic constant measurements are presented in the Appendix.

II. EXPERIMENT

The emphasis of the present work is on the analysis of the elastic properties of $CsNiCl_3$ obtained via ultrasonic velocity measurements as a function of temperature and magnetic field.[9,16] Data were collected using a high-resolution pulsed ultrasonic interferometer operating at 30 MHz. Measurements were carried out on a single crystal with a length of 8.9 mm along the c axis and approximately 2.5 mm along the perpendicular directions. Data associated with the elastic constant C_{33} were determined using longitudinal modes propagating along the c axis, while transverse lithium niobate transducers were used in order to measure C_{66}. These data were also used to determine the magnetic phase diagram of $CsNiCl_3$ for a field applied along the c axis. The phase diagram shown in Fig. 1 agrees well with previous measurements obtained at lower fields.[27–29]

III. MODEL

The derivation presented here is essentially based on the formulation of a nonlocal Landau free energy which is known to successfully account for the phase diagrams of many magnetic systems with a triangular lattice, for example, $CsNiCl_3$, $CsNiF_3$, and $CsMnBr_3$.[4,5,8] Thus, our approach is to incorporate magnetoelastic coupling terms to the existing model by Plumer *et al.* [5] These contributions are essential in order to account for the field and temperature dependence of the elastic constants measured in $CsNiCl_3$.[9,16] In this context, the total free energy F is decomposed into three contributions, expressed as[8]

$$F = F_s + F_{es} + F_e. \tag{1}$$

Here, the spin-only part of the free energy F_s, given in Eq. (2), is represented by a Taylor expansion in term of the components of the spin density $\mathbf{s}(\mathbf{r})$. Using the same approach,[8] the magnetoelastic energy F_{es} is defined in Eq. (3). As our analysis indicates, linear-quadratic and biquadratic coupling terms between the strain components e_{ij} and the spin density $\mathbf{s}(\mathbf{r})$ are both necessary. Finally, the integral form of the elastic energy F_e, defined in terms of the elastic constants C_{ijkl}, is

given in Eq. (4).

$$F_s = \frac{1}{2V}\int d\mathbf{r_1}d\mathbf{r_2}J_{ij}(\mathbf{r_1},\mathbf{r_2})s_i(\mathbf{r_1})s_j(\mathbf{r_2}) + \frac{1}{4V}\int d\mathbf{r_1}d\mathbf{r_2}d\mathbf{r_3}d\mathbf{r_4}B_{ijkl}(\mathbf{r_1},\mathbf{r_2};\mathbf{r_3},\mathbf{r_4})s_i(\mathbf{r_1})s_j(\mathbf{r_2}) \times s_k(\mathbf{r_3})s_l(\mathbf{r_4}) - \int \mathbf{s}(\mathbf{r})\cdot\mathbf{H}\,d\mathbf{r}, \quad (2)$$

$$F_{es} = \frac{1}{2V}\int d\mathbf{r_1}d\mathbf{r_2}d\mathbf{r_3}K_{ijkl}(\mathbf{r_1};\mathbf{r_2},\mathbf{r_3})e_{ij}(\mathbf{r_1})s_k(\mathbf{r_2})s_l(\mathbf{r_3}) + \frac{1}{4V}\int d\mathbf{r_1}d\mathbf{r_2}d\mathbf{r_3}d\mathbf{r_4}V_{ijklmn}(\mathbf{r_1},\mathbf{r_2};\mathbf{r_3},\mathbf{r_4})e_{ij}(\mathbf{r_1}) \times e_{kl}(\mathbf{r_2})s_m(\mathbf{r_3})s_n(\mathbf{r_4}), \quad (3)$$

$$F_e = \frac{1}{2V^2}\int d\mathbf{r_1}d\mathbf{r_2}C_{ijkl}e_{ij}(\mathbf{r_1})e_{kl}(\mathbf{r_2}). \quad (4)$$

Here, the summation convention of repeated indices is adopted, with $i,j,k,l,m,n = x,y,z$. Moreover, we assume that all coupling coefficients J_{ij}, B_{ijkl}, K_{ijkl}, and V_{ijklmn} depend on the spin separation $\tau_{\mathbf{ij}} = \mathbf{r_i} - \mathbf{r_j}$. The total free energy must be invariant with respect to the hexagonal D^4_{6h} symmetry operations. For example, the existence of an inversion symmetry center imposes that $J_{ij}(\tau) = J_{ij}(-\tau)$, while the time reversal property is only satisfied by even powers of the spin density. The other crystal symmetry operations impose additional restrictions which considerably reduce the number of coupling terms. A general discussion of these techniques is given in Ref. 4. These independent contributions are then evaluated considering that the local magnetic moment density $\mathbf{s}(\mathbf{r})$ is defined relative to a nonlocal spin density $\rho(\mathbf{r})$ such that

$$\mathbf{s}(\mathbf{r}) = \frac{V}{N}\sum_R \rho(\mathbf{r})\delta(\mathbf{r}-\mathbf{R}), \quad (5)$$

with $\mathbf{R}$ representing lattice vectors and N the number of Ni^{2+} magnetic ions. As in Ref. 5, we assume that the antiferromagnetic part of the spin density is appropriately characterized by a single $\mathbf{Q}$ vector according to

$$\rho(\mathbf{r}) = \mathbf{m} + \mathbf{S}e^{i\mathbf{Q}\cdot\mathbf{r}} + \mathbf{S}^* e^{-i\mathbf{Q}\cdot\mathbf{r}}, \quad (6)$$

where $\mathbf{S}$ is the spin polarization vector and $\mathbf{m}$ is the induced magnetization. In order to account for nonlinear spin configurations, the spin polarization vector is expressed as

$$\mathbf{S} = \mathbf{S_1} + i\mathbf{S_2}, \quad (7)$$

where the polarization vectors $\mathbf{S_1}$ and $\mathbf{S_2}$ are defined as

$$\mathbf{S_1} = S\cos\beta[\sin\theta\hat{\rho}_\mathbf{1} + \cos\theta\hat{\mathbf{z}}] \quad \text{and} \quad \mathbf{S_2} = S\sin\beta\hat{\rho}_\mathbf{2}, \quad (8)$$

with $\hat{\mathbf{z}}$ pointing along the c axis while the arbitrary orthogonal unit vectors $\hat{\rho}_\mathbf{1}$ and $\hat{\rho}_\mathbf{2}$ lie in the basal planes. To properly account for the magnetoelastic coupling, it is important to define the spin orientation relative to the crystallographic directions; for that reason we define

$$\hat{\rho}_\mathbf{1} = \cos\phi\hat{\mathbf{x}} + \sin\phi\hat{\mathbf{y}} \quad \text{and} \quad \hat{\rho}_\mathbf{2} = -\sin\phi\hat{\mathbf{x}} + \cos\phi\hat{\mathbf{y}}. \quad (9)$$

Here, the angle ϕ is defined relative to the hexagonal lattice vectors, $\hat{\mathbf{a}} = \hat{\mathbf{y}}$.

For a magnetic field applied along the z direction, the free energy reduces to

$$F_s = (A_Q - A_z\zeta^2)S^2 + \tfrac{1}{2}BS^4 + A_z\zeta^2S_\perp^2 + 2B_2(S_\perp^2 - S^2)S_\perp^2 + \tfrac{1}{2}A_o m_z^2 + \tfrac{1}{4}B_3 m_z^4 + B_5 m_z^2 S^2 + 2B_4\zeta^2(S^2 - S_\perp^2)m_z^2 - m_z H, \quad (10)$$

$$F_{es} = F_{es;K} + F_{es;V}, \quad (11)$$

$$F_{es;K} = (2K_{11}(S_\perp^2\zeta^2 + S^2(1-\zeta^2)) + 2K_{13}(S^2 - S_\perp^2)\zeta^2)(e_{11}+e_{22}) + (2K_{31}(S_\perp^2\zeta^2 + S^2(1-\zeta^2)) + 2K_{33}(S^2 - S_\perp^2)\zeta^2)e_{33} + 2K_{66}(S_\perp^2(\zeta^2-2) + S^2(1-\zeta^2))\cos[2\phi](e_{11}-e_{22}) + 4K_{66}(S_\perp^2(\zeta^2-2) + S^2(1-\zeta^2))\sin[2\phi]e_{12} + \widetilde{K}_{13}m_z^2(e_{11}+e_{22}) + \widetilde{K}_{33}m_z^2 e_{33}, \quad (12)$$

$$F_e = \tfrac{1}{2}C_{11}\left(e_{11}^2 + e_{22}^2\right) + \tfrac{1}{2}C_{33}e_{33}^2 + 2C_{44}\left(e_{13}^2 + e_{23}^2\right) + 2C_{66}e_{12}^2 + C_{12}e_{11}e_{22} + C_{13}(e_{11}+e_{22})e_{33}, \quad (13)$$

where $A_Q = a(T - T_Q)$, $A_o = a(T - T_o)$, $S_\perp = S\sin\beta$, and $\zeta = \cos\theta$. The order parameters S, $S_\perp$, and ζ are associated with the linear, elliptical, and 120° phases identified in Fig. 1. Using the expression of $\mathbf{s}(\mathbf{r})$ in Eq. (3), along with the fact that $e_{ij} = e_{ji}$, we also determined the allowed coupling terms between the strains and the order parameters. Equation (12) gives the expression for the linear-coupling terms, where

$$K_{ij} = \frac{V}{N}\sum_\mathbf{R} K_{iijj}e^{i\mathbf{Q}\cdot\mathbf{R}},$$

$$\widetilde{K}_{ij} = \frac{V}{N}\sum_\mathbf{R} K_{iijj},$$

$$\frac{1}{N}\sum_\mathbf{R} e^{i2\mathbf{Q}\cdot\mathbf{R}} = \Delta_{2\mathbf{Q},\mathbf{G}} = 0. \quad (14)$$

In the case of $CsNiCl_3$, as the spin polarization wave vector, $\mathbf{Q} = 4\pi/3a\hat{\mathbf{y}}$, does not coincide with any of the reciprocal lattice vectors $\mathbf{G}/2$, none of the coupling terms proportional to the Kronecker Δ function $\Delta_{2\mathbf{Q},\mathbf{G}}$ are allowed.

The biquadratic coupling terms $F_{es;V}$ have also been derived. As reported in Table I, there are 14 terms associated with the order parameters and 5 terms related to the induced magnetization. Finally, the form of the elastic energy determined by the hexagonal point-group symmetry corresponds to Eq. (13).

TABLE I. Biquadratic coupling terms between the order parameters $(S, S_\perp, \zeta)$, the magnetization m_z, and the strain components e_{ij}.

1.	$2V_{333}(S^2 - S_\perp^2)\zeta^2 e_{33}^2$	1.	$\widetilde{V}_{333} m_z^2 e_{33}^2$
2.	$4V_{133}(S^2 - S_\perp^2)\zeta^2(e_{11} + e_{22})e_{33}$	2.	$2\widetilde{V}_{133} m_z^2(e_{11} + e_{22})e_{33}$
3.	$2V_{113}(S^2 - S_\perp^2)\zeta^2(e_{11} + e_{22})^2$	3.	$\widetilde{V}_{113} m_z^2(e_{11} + e_{22})^2$
4.	$8V_{553}(S^2 - S_\perp^2)\zeta^2(e_{13}^2 + e_{23}^2)$	4.	$4\widetilde{V}_{553} m_z^2(e_{13}^2 + e_{23}^2)$
5.	$8V_{663}(S^2 - S_\perp^2)\zeta^2(e_{12}^2 - e_{11}e_{22})$	5.	$4\widetilde{V}_{663} m_z^2(e_{12}^2 - e_{11}e_{22})$
6.	$2V_{331}(S_\perp^2\zeta^2 + S^2(1-\zeta^2))e_{33}^2$		
7.	$2(V_{131} + V_{231})(S_\perp^2\zeta^2 + S^2(1-\zeta^2))(e_{11} + e_{22})e_{33}$		
8.	$4(V_{441} + V_{551})(S_\perp^2\zeta^2 + S^2(1-\zeta^2))(e_{13}^2 + e_{23}^2)$		
9.	$1/2(V_{111} + V_{221} + 2V_{121})(S_\perp^2\zeta^2 + S^2(1-\zeta^2))(e_{11} + e_{22})^2$		
10.	$1/4(V_{111} + V_{221} - 2V_{121} + 4V_{661})(S_\perp^2\zeta^2 + S^2(1-\zeta^2))(e_{11}^2 + 4e_{12}^2 - 2e_{11}e_{22} + e_{22}^2)$		
11.	$2(V_{131} - V_{231})(S^2(1-\zeta^2) - S_\perp^2(2-\zeta^2))(\cos[2\phi]e_{11}e_{33} + 2\sin[2\phi]e_{12}e_{33} - \cos[2\phi]e_{22}e_{33})$		
12.	$4(V_{551} - V_{441})(S^2(1-\zeta^2) - S_\perp^2(2-\zeta^2))(\cos[2\phi]e_{13}^2 + 2\sin[2\phi]e_{13}e_{23} - \cos[2\phi]e_{23}^2)$		
13.	$(V_{111} - V_{221})(S^2(1-\zeta^2) - S_\perp^2(2-\zeta^2))(e_{11} + e_{22})(\cos[2\phi]e_{11} + 2\sin[2\phi]e_{12} - \cos[2\phi]e_{22})$		
14.	$1/4(V_{111} + V_{221} - 2V_{121} - 4V_{661})(S^2(1-\zeta^2) - S_\perp^2(2-\zeta^2))$ $(\cos[2\phi]e_{11}^2 - 4\cos[2\phi]e_{12}^2 + 4\sin[2\phi]e_{12}e_{22} + \cos[2\phi]e_{22}^2 - 2e_{11}(2\sin[2\phi]e_{12} + \cos[2\phi]e_{22}))$		

IV. MAGNETIC PHASE DIAGRAM

The total free energy defined by Eqs. (10)–(13), along with the biquadratic coupling terms listed in Table I, can be used to account for the magnetic phase diagram of $CsNiCl_3$ as well as the elastic properties as a function of field and temperature. It is straightforward to show that the effect of the magnetoelastic coupling terms [Eq. (12)] is to renormalize the coefficients of the Landau free energy F_s. Moreover, these effects scale with the elastic variations observed in the magnetic states. As these variations are small ($\Delta C/C \sim 10^{-4}$), it is still justified to determine the magnetic phase diagram by minimizing the Landau free energy F_s alone with respect to the order parameters. Details regarding this derivation can be found in Ref. 5. For convenience, derivations of the phase boundaries are reproduced in the Appendix for $H \parallel c$. Using the analytical solutions [Eqs. (A4)] along with the numerical values listed in Table III, it is then possible to obtain very good agreement with the experimental data as shown in Fig. 1.

As the coefficients in Table III are preset by fitting the phase diagram, the significance of the model can be put to the test by comparing the calculated magnetization with the experimental data collected at 2.25 K by Johnson *et al.*[27] Shown in Fig. 2 are the numerical prediction (solid line) and the measured magnetization. As usual, due to fluctuation phenomena, the data show a gradual variation around the spin-flop first-order transition, while the mean-field model displays a small discontinuity at the critical field $H = 2.0$ T. The inset in Fig. 2 also shows the field dependence of the susceptibility. Here, the solid line corresponds to a fit obtained using a single Gaussian function center at the critical field. The fitted susceptibility is used later for analysis of the elastic constants.

V. ELASTIC PROPERTIES

We now focus our attention on the field and temperature dependence of elastic properties of $CsNiCl_3$. Minimizing the total free energy with respect to the strain components, we obtain the relations

$$
\begin{aligned}
e_{11} + e_{22} &= -\frac{\widetilde{K}_{13} m_z^2 + 2(K_{13}(S^2 - S_\perp^2)\zeta^2 + K_{11}(S_\perp^2\zeta^2 + S^2(1-\zeta^2)))}{(C_{11} + C_{12})/2}, \\
e_{11} - e_{22} &= -\frac{4K_{66}(S^2(1-\zeta^2) - S_\perp^2(2-\zeta^2))\cos[2\phi]}{C_{11} - C_{12}}, \\
e_{33} &= -\frac{\widetilde{K}_{33} m_z^2 + 2(K_{33}(S^2 - S_\perp^2)\zeta^2 + K_{31}(S_\perp^2\zeta^2 + S^2(1-\zeta^2)))}{C_{33}}, \\
e_{23} &= 0, \\
e_{13} &= 0, \\
e_{12} &= -\frac{2K_{66}(S^2(1-\zeta^2) - S_\perp^2(2-\zeta^2))\sin[2\phi]}{C_{66}}.
\end{aligned}
\tag{15}
$$

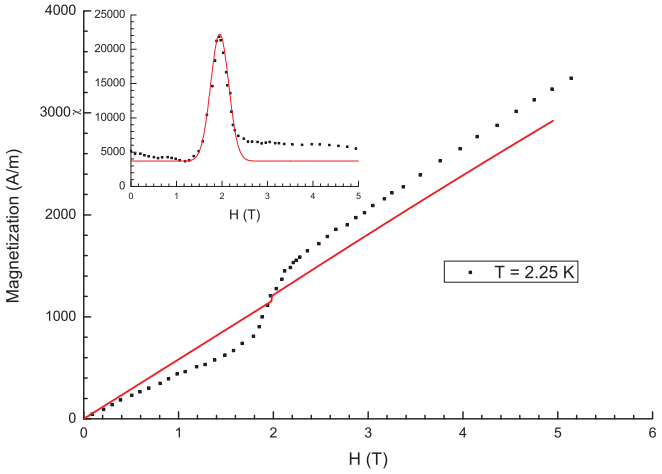

FIG. 2. (Color online) Field dependence of the magnetization of $CsNiCl_3$ calculated at 2.25 K for $\mathbf{H}\|\hat{\mathbf{c}}$. The numerical prediction [solid (red) line] is compared to data measured by Johnson *et al.*[27] Inset: Field dependence of the susceptibility at 2.25 K based on the data of Johnson *et al.* [27] along with the Gaussian fit [solid (red) line].

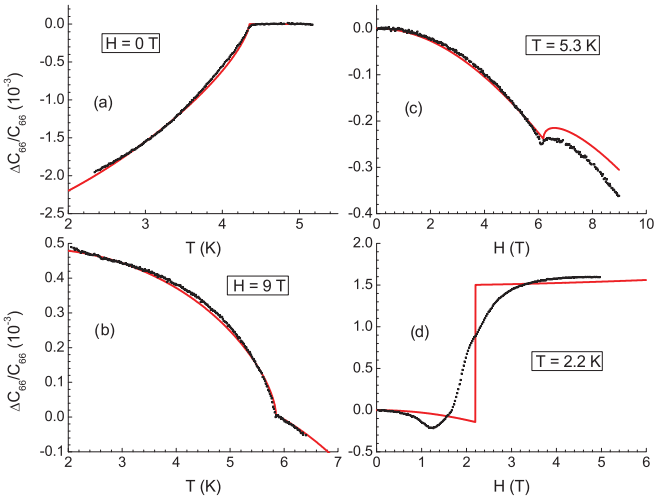

FIG. 3. (Color online) Relative variation of the elastic constant C_{66} as a function of temperature or magnetic field. Experimental data are represented by symbols, while solid (red) lines represent numerical predictions based on parameters and solutions listed in Table II.

Since ϕ corresponds to the angle between the basal-plane spin polarization relative to the lattice vectors, we note that for an arbitrary angle ϕ, the magnetic transitions would lead to a structural transformation due to the shear deformation associated with $e_{12} \neq 0$. In this case the structural symmetry would be reduced to monoclinic. However, based on the analysis reported by Zhu *et al.*,[30] it is energetically favorable to have the spin polarization $\mathbf{S}$ confined to the $z\rho_2$ plane in the elliptical phase. Thus, as in Ref. 30, we assign $\hat{\rho}_2$ to the Cartesian direction $\hat{\mathbf{y}}$, which coincides with the hexagonal a axis. For that reason, we limit our analysis to the case where $\phi = 0$ [see Eq. (9)].

Using the total free energy, solutions for the elastic constants are obtained using[31]

$$C^*_{mn} = \frac{\partial^2 F}{\partial e_m \partial e_n} - \frac{\partial^2 F}{\partial O \partial e_m}\left(\frac{\partial^2 F}{\partial O^2}\right)^{-1}\frac{\partial^2 F}{\partial e_n \partial O} - \frac{\partial^2 F}{\partial m_z \partial e_m}\left(\frac{\partial^2 F}{\partial m_z^2}\right)^{-1}\frac{\partial^2 F}{\partial e_n \partial m_z}, \quad (16)$$

where O represents the order parameter associated with a specific magnetic phase transition. Our analysis focuses on the temperature and field dependence of C_{33} and C_{66}, as shown in Figs. 3 and 4. Thus, solutions for these two moduli are listed in Table II, while details regarding how the value of the coupling coefficients are determined can be found in the Appendix.

The predictions for C_{66} are particularly interesting. As only quadratic-quadratic coupling terms are allowed for e_{12} [$\phi = 0$ in Eq. (12)], the temperature dependence of C_{66} is proportional to the order parameter squared, while the field dependence scales with m_z^2 (Table II). At zero field, the data display a very small variation signaling the paramagnetic-linear phase transition at $T_{N_1} = 4.75$ K [not clearly visible in Fig. 3(a)]. However, below the linear-elliptical phase transition ($T_{N_2} = 4.35$ K), the observed temperature dependence is consistent with that of $S_\perp^2$. In order to optimize the agreement with the experimental data shown in Figs. 3 and 4, the usual mean-field temperature dependence of the order parameter $S_\perp$ is replaced by the phenomenological relation given by

$$S_\perp(T) = \alpha\left\{\theta_s\left[\coth\left(\frac{\theta_s}{T_N}\right) - \coth\left(\frac{\theta_s}{T}\right)\right]\right\}^\beta. \quad (17)$$

This form has been used by other groups to account for the saturation of the order parameter observed at low temperatures for structural phase transitions which are well characterized with a mean-field critical exponent $\beta = 0.5$.[32–34] As a low-order expansion of the free energy in powers of S^2, the Landau free energy in its traditional form has a range of validity in regions of the phase diagram only close to the paramagentic phase boundary where S^2 is small. Equation (16) is essentially

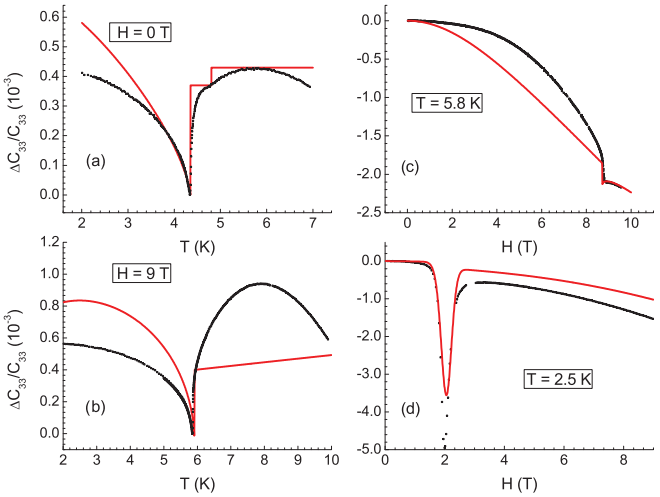

FIG. 4. (Color online) Relative variation of the elastic constant C_{33} as a function of temperature or magnetic field. Experimental data are represented by symbols, while solid (red) lines represent numerical predictions based on parameters and solutions listed in Table II.

TABLE II. Solutions for elastic modulii C_{33} and C_{66} with numerical values of the coupling coefficients.

$C_{33}(\mathrm{P}) = C_{33} - 4\widetilde{K}_{33}^2 m_z^2 \chi + 2\widetilde{V}_{333} m_z^2$	$C_{33} = 6.16 \times 10^{10}$ N/m^2
$C_{33}(\mathrm{L}) = C_{33}(\mathrm{P}) - \frac{4K_{33}^2}{B} + 4V_{333}S^2$	$\widetilde{K}_{33} = -0.11$
$C_{33}(\mathrm{E}) = C_{33}(\mathrm{L}) - \frac{(K_{31}-K_{33})^2}{B_2} + 4S_\perp^2(V_{331} - V_{333})$	$\widetilde{V}_{333} = 8.67$
$C_{33}(\mathrm{SF}) = \mathrm{C}_{33}(\mathrm{P}) - \frac{4\mathrm{K}_{31}^2}{\mathrm{B}-\mathrm{B}_2} + 8\mathrm{V}_{331}\mathrm{S}_\perp^2$	$K_{33} = 0.0025$
	$K_{31} = -0.0029$
	$V_{333} = 0$
	$V_{331} = 0.30$
$C_{66}(\mathrm{P}) = C_{66} + 2\widetilde{V}_{663} m_z^2$	$C_{66} = 3.56 \times 10^{10}$ N/m^2
$C_{66}(\mathrm{L}) = C_{66}(\mathrm{P}) + 4V_{663}S^2$	$\widetilde{V}_{663} = -0.52$
$C_{66}(\mathrm{E}) = C_{66}(\mathrm{L}) + (V_{12} - 4V_{663})S_\perp^2 \neq \frac{C_{11}(E)-C_{12}(E)}{2}$	$V_{663} = 0$
$C_{66}(\mathrm{SF}) = \mathrm{C}_{66}(\mathrm{P}) + (\mathrm{V}_{12} + 4\mathrm{V}_{661})\mathrm{S}_\perp^2$	$V_{12} = V_{111} - 2V_{121} + V_{221} = -2.64$
	$V_{661} = 0.77$

a mean-field result for Ising-like systems which does not have this restriction. In the case of $CsNiCl_3$, the proposed phenomenological function [Eq. (17)] has the advantage to reproduce the critical behavior close to T_N as well as to mimic the lower-T saturation effect by setting $\theta_s = 0.5T_N$. For the purposes of the analysis, we used $\beta = 0.35$ in the linear and elliptical phases, while for the 120° phase, $\beta \sim 0.30$. These values correspond to those determined in Ref. 16.

Using Eq. (17) with the numerical values listed in Table II, it is then possible to obtain excellent agreement with the temperature dependence of C_{66} measured at 0 and 9 T [Figs. 3(a) and 3(b)]. The field dependence of C_{66} is related to the parameter $\widetilde{V}_{663}$, which is easily determined using the variation observed in the paramagnetic phase (see Appendix for details). As shown in Fig. 3(d), the model properly accounts for the increase in C_{66} at the spin-flop phase transition ($H_{\mathrm{SF}} \approx 2$ T). According to our analysis, this variation is associated with the change in the magnetoelastic coupling constant ($4V_{661}$) as the spin system transforms from an xz-plane polarization (elliptical phase) into an xy-plane configuration in the 120° phase. Surprisingly, variations due to discontinuity in $S_\perp$ and m_z are an order of magnitude smaller. In addition, the field dependence measured at $T = 5.3$ K [Fig. 3(c)] is also well reproduced, giving further support to the model. In particular, it reproduces the unusual anomaly observed at the paramagnetic-120° phase boundary.

We now focus on the analysis of the temperature and field dependence of C_{33} presented in Fig. 4. At zero field [Fig. 4(a)], the onset of the long-range linear antiferromagnetic ordering corresponds to a small slope variation in the data at T_{N_1}, while the elliptical magnetic ordering is easily identified by a pronounced anomaly at T_{N_2}. The comparison with the model predictions indicates that linear-quadratic coupling terms account for the discontinuous variation at the critical temperatures, while biquadratic terms are necessary in order to qualitatively reproduce the temperature dependence observed at lower temperatures. Thus, the variation of C_{33} for $T < T_{N2}$ is associated with that of $S_\perp^2$ given by Eq. (17), while the coupling with S^2 is negligible ($V_{333} = 0$). Again, details regarding how the magnetoelastic constants are determined are given in the Appendix. With all coefficients set, the numerical predictions are compared to results obtained as a function of temperature for $H = 0$ and 9 T, as well as measurements versus the field for $T = 2.5$ and 5.8 K. The fact that the agreement at $H = 0$ T [Fig. 4(a)] is not as good as for C_{66} might reflect that higher order coupling terms have a significant contribution in the case of longitudinal modes. In Figs. 4(b) and 4(c), while the agreement is qualitative, we also notice significant deviations, in particular, for the paramagnetic state. We attribute these discrepancies to spin fluctuations (beyond mean field), which are known to be important along the easy axis of quasi-one-dimensional magnetic systems such as $CsNiCl_3$.[35,36] The results presented in Fig. 4(d) are especially interesting, as it shows the field dependence of C_{33} at the spin-flop phase boundary. As predicted in Table II, the minimum on C_{33}, associated with the term $-4\widetilde{K}_{33}^2 m_z^2 \chi$, reflects the field dependence of the magnetic susceptibility around the phase transition. For the numerical prediction [solid (red) line], the fit of the susceptibility data measured at $T = 2.25$ K and shown in Fig. 2 has been used. Note that the coupling constant $\widetilde{K}_{33}$ is determined from magnetostriction measurements,[37] independent of our elastic constant measurements shown in Fig. 4 (see the Appendix). A similar field dependence has also been observed in the velocity of longitudinal modes in $(VO)_2P_2O_7$.[38] In summary, while the agreement with the model predictions is not as good as for C_{66}, the model does capture the distinct features observed on both modulii.

As a final test, we present in Fig. 5 the numerical predictions for the temperature dependence of the thermal expansion coefficients $\alpha_1 = de_1/dT$ and $\alpha_3 = de_3/dT$ for $H = 0$. The predictions derived from Eq. (15) compare well with the experimental data shown in Refs. 9 and 39, where $\alpha_\parallel = \alpha_3$ and $\alpha_\perp = \alpha_1$. Note that the prediction for α_3 is obtained without adjusting any coefficient, while the experimental data for α_1, which show only one anomaly at T_{N_2}, indicate that the coupling constant $K_{13} \simeq 0$. This constant characterizes the effect of the spin z component and the basal plane deformations (e_1, e_2). This observation is also confirmed by sound velocity measurements[9] which show no anomaly at T_{N_1} for longitudinal modes propagating into the basal plane.

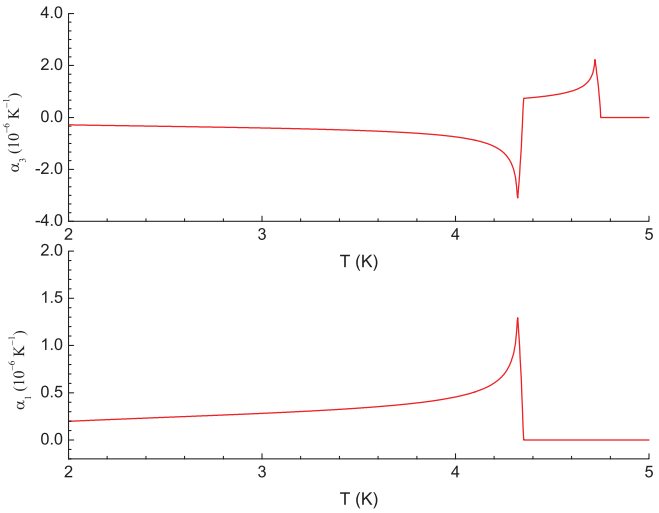

FIG. 5. (Color online) Numerical predictions of the low-temperature thermal expansion coefficients α_3 and α_1 for $CsNiCl_3$.

VI. CONCLUSION

In this investigation, we present a Landau model free energy of magnetoelastic coupling derived from symmetry arguments that complements and extends our earlier work.[16] The model predictions are tested by correlating a substantial set of experimental data on $CsNiCl_3$ such as the magnetic phase diagram, magnetization, thermal expansion coefficients, and elastic constants, measured as a function of temperature and field. In general, the model captures well the types of anomalies observed at the different phase boundaries. Moreover, we show that the anomaly observed on C_{33} as a function of the field for $T = 2.5$ K [Fig. 4(d)] is dominated by the field dependence of the magnetic susceptibility. On the other hand, results obtained for C_{66} [Fig. 3(d)] instead display a step-like anomaly at the phase transition. Based on the numerical analysis, we conclude that this variation is associated with the change in the magnetoelastic coupling for different spin configurations. The discontinuities of the order parameter $S_\perp$ and m_z (see Fig. 2) seem to play a secondary role. Note that the same approach has been used to analyze the magnetoelastic coupling in the magnetoelectric compound $CuFeO_2$[40–42] and can be applied to other triangular antiferromagnets. It can also be used for any magnetic phase transitions.

Based on the model presented in this paper, it is also possible to deduce the crystal symmetry. As mentioned earlier, the analysis done by Zhu *et al.*[30] shows that it is energetically favorable to have the basal plane spin polarization pointing along the crystallographic direction a. Consequently, at low fields the spin polarization vector $\mathbf{S}$ is confined in the yz plane with the modulation vector $\mathbf{Q}$ parallel to the y direction ($\mathbf{Q} = 4\pi/3a\hat{\mathbf{y}}$). Thus, depending on the spin configuration, some symmetry elements might be lost, leading to a structural change. Information regarding this possibility can be obtained via the analysis of the magnetoelastic coupling. On one hand, based on the solution for $e_{11} - e_{22}$ [Eq. (15)], we see that the order parameter associated with the elliptical phase, $S_\perp \neq 0$ with $\zeta = 1$, could lead to a structural deformation from hexagonal to orthorhombic. On the other hand, the symmetry of the linear phase ($S_\perp = 0$ with $\zeta = 1$) and that of the 120° phase ($S = \sqrt{2}S_\perp$ with $\zeta = 0$) should remain hexagonal ($e_{11} - e_{22} = 0$). Thus, based on our analysis, one would expect to observe a structural change at the linear-elliptical phase transition. However, considering that the magnetoelastic effects in $CsNiCl_3$ are small below T_{N_2} ($e_1 \sim e_2 \sim 10^{-6}$), this symmetry change might be difficult to detect. Note that the symmetry designations mentioned here are also consistent with the number of independent elastic constants obtained for each symmetry. While no additional elastic constants are obtained for the linear and 120° phase, a total of nine independent constants are evident for the elliptical phase. In particular, we obtain that C_{66} is no longer equal to $(C_{11} - C_{12})/2$, indicating that the hexagonal symmetry is clearly broken in the elliptical phase. Finally, we stress that linear-quadratic and biquadratic coupling terms are both necessary in order to account for the elastic properties of $CsNiCl_3$ as well as a likely symmetry change.

ACKNOWLEDGMENTS

This work was supported by grants from the Natural Science and Engineering Research Council of Canada (NSERC) and the Canada Foundation for Innovation (CFI).

APPENDIX

Considering that the derived Landau free energy contains a large number of adjustable coefficients, it is crucial to rely on a sufficiently large pool of independent experimental data. Thus in this Appendix, we show how all coefficient values are determined using data associated with the magnetic phase diagram, magnetization, strains, and elastic constants.

Considering that the elastic energy variation in $CsNiCl_3$ is small at low temperatures, we determine the magnetic phase by minimizing the Landau free energy F_s [Eq. (10)]. In that context, the derivation presented here reduces to that realized by Plumer *et al.*[5] for $H \parallel c$. Thus, minimization of F_s with respect to the magnetization m_z and the order parameters S and $S_\perp$ gives

$$\begin{aligned}
\partial F_s/\partial S &= \left(A_Q + 2B_5 m_z^2 - 2B_2 S_\perp^2 + BS^2 \right.\\
&\quad \left. + \left(2B_4 m_z^2 - A_z\right)\zeta^2\right) S = 0,\\
\partial F_s/\partial S_\perp &= \left(2B_2(2S_\perp^2 - S^2) + \left(A_z - 2B_4 m_z^2\right)\zeta^2\right) S_\perp = 0,\\
\partial F_s/\partial m_z &= -H + A_0 m_z + B_3 m_z^3 + 2B_5 m_z S^2\\
&\quad + 4B_4 m_z (S^2 - S_\perp^2)\zeta^2 = 0.
\end{aligned} \tag{A1}$$

Inspection of Eqs. (A1) reveals four possible magnetic states, corresponding to

$$\begin{array}{llll}
\text{P state:} & S = 0, & S_\perp = 0, & \zeta = 1.\\
\text{L state:} & S \neq 0, & S_\perp = 0, & \zeta = 1.\\
\text{E state:} & S \neq 0, & S_\perp \neq 0, & \zeta = 1.\\
120^\circ \text{ state:} & S = \sqrt{2}S_\perp, & S_\perp \neq 0, & \zeta = 0.
\end{array} \tag{A2}$$

Here, the labels P, L, E, and 120° are used to identify the paramagnetic, linear, elliptical, and 120° spin configurations. Moreover, we note that the order parameter ζ is associated with the spin-flop phase transition between the elliptical and the 120° phase, which is first order in nature. The critical temperatures at zero field are easily obtained by considering

that $S = 0$ at T_{N_1} while $S_\perp = 0$ at T_{N_2}. Furthermore, the coordinates of the multicritical point are deduced by imposing that S and $S_\perp$ are both 0 at (T_m, H_m). Thus, from Eqs. (A1) we obtain that

$$\begin{aligned} T_{N_1} &= T_Q + \frac{A_z}{a}, \\ T_{N_2} &= T_{N_1} - \frac{B}{2B_2}\frac{A_z}{a}, \\ T_m &= T_{N_1} - \frac{B_6}{2B_4}\frac{A_z}{a}, \\ H_m &= \sqrt{\frac{A_z}{2B_4}}\left(a(T_Q - T_o) + \frac{(B_3 - B_5)}{2B_4}A_z\right), \end{aligned} \tag{A3}$$

where $B_6 = 2B_4 + B_5$, $B_7 = BB_4/B_2 - B_6$, and $B_8 = B_3 - 2B_6^2/B$. Likewise, analytical solutions for the continuous phase boundaries H_{N_1}, H_{N_2}, and H_c are obtained by solving Eq. (A1). These solutions, defining the $P \to L$, the $L \to E$, and the $P \to 120^\circ$ phase boundaries are conveniently written as

$$\begin{aligned} H_{N_1} &= \sqrt{\frac{-A_1}{B_6}}\left(A_o - \frac{B_3}{B_6}A_1\right), \\ H_{N_2} &= \sqrt{\frac{A_2}{B_7}}\left(A_o - \frac{2B_6}{B}A_1 + \frac{B_8}{B_7}A_2\right), \\ H_c &= \sqrt{\frac{-A_Q}{B5}}\left(A_o - \frac{B_3}{B_5}A_Q\right), \end{aligned} \tag{A4}$$

where $A_1 = a(T - T_{N_1})$, $A_2 = a(T - T_{N_2})$, $A_o = a(T - T_o)$. Inspection of the solution for H_c shows that the parameter $T_Q = 4.4$ K corresponds to the temperature at which the phase boundary H_c extrapolates to $H = 0$. Moreover, T_o can be estimated considering that the magnetic susceptibility in the paramagnetic phase is given by

$$\chi = \frac{1}{\partial^2 F_s/\partial m_z^2} = \frac{1}{a(T - T_o)}. \tag{A5}$$

Thus, the parameter $T_o = -70$ K corresponds to the value of the experimental curie temperature[43] for $CsNiCl_3$, while the coefficient a is determined by scaling the calculated magnetization with the experimental data shown in Fig. 2. The last boundary, which defines the E $\to 120^\circ$ first-order phase transition ($\zeta = 1 \to 0$), is obtained numerically by comparing the free energy of both phases. Imposing that $T_{N_1} = 4.75$ K, $T_{N_2} = 4.38$ K, $T_m = 4.52$ K, $H_m = 2.3$ T, $H_{SF}(0K) = 1.6$ T, and $H_c(5.8K) = 8.5$ T, we obtain the numerical values reported in Table III. As shown in Fig. 4, the analytical solutions, Eqs. (A4) (while the H_{SP} phase boundary is determined numerically), combined with the values reported in Table III are sufficient to reproduce the magnetic phase diagram of $CsNiCl_3$ up to 10 T.

In a similar manner, the magnetoelastic coefficients listed in Table II are determined by imposing constrains consistent with variations of the elastic properties. Thus, according to the analytical solution given in Table II, the temperature of C_{66} is proportional to S^2 and $S_\perp^2$, while the field dependence scales with m_z^2. At zero field, the data display a very small variation signaling the paramagnetic-linear phase transition

TABLE III. Numerical values used to calculate the phase boundaries presented in Fig. 1.

a	2.59×10^{-5}
T_o	-70
T_Q	4.4
A_z/a	0.40
B	3.21×10^{-12}
B_2/B	0.50
B_3/B	15.4
B_4/B	1.21
B_5/B	-1.03

at $T_{N_1} = 4.75$ K [not clearly visible in Fig. 3(a)]. Thus, as indicated by the list of numerical constraints [see Eqs. (A6)], we conclude that $V_{663} \simeq 0$, while the temperature dependence observed below the linear-elliptical phase transition (below $T_{N_2} = 4.35$ K) is adjusted using the constant V_{12}. The field dependence of C_{66} in the paramagnetic state at $T = 5.3$ K [Fig. 3(c)] is then used to determine $\tilde{V}_{663}$, while the last coupling constant V_{661} is set using the data obtained at $H = 9$ T [Fig. 3(b)].

$$\begin{aligned} C_{66}(L) - C_{66}(P) &= 4V_{663}S^2 \simeq 0 \\ \frac{\Delta C_{66}}{C_{66}}(3K) &= \frac{V_{12}}{C_{66}}S_\perp^2 = -1.55 \times 10^{-3} \\ \frac{\Delta C_{66}}{C_{66}}(5.3K,5T) &= \frac{2\tilde{V}_{663}}{C_{66}}m_z^2 = -1.5 \times 10^{-4} \\ \frac{\Delta C_{66}}{C_{66}}(2K,9T) &= -\frac{(V_{12} + 4V_{661})}{C_{66}}S_\perp^2 = -4.8 \times 10^{-4} \end{aligned} \tag{A6}$$

The magnetoelastic coefficients associated with C_{33} are determined using the numerical constraints list in Eqs. (A7).

$$\begin{aligned} \frac{\Delta C_{33}}{C_{33}}(T_{N_1}) &= -\frac{4K_{33}^2}{BC_{33}} = -0.06 \times 10^{-3} \\ \frac{\Delta C_{33}}{C_{33}}(T_{N_2}) &= -\frac{(K_{31} - K_{33})^2}{B_2C_{33}} = -0.37 \times 10^{-3} \\ \frac{\Delta C_{33}}{C_{33}}(3.5K) &= \frac{4V_{331}}{C_{33}}S_\perp^2 = 0.33 \times 10^{-3} \\ e_{33}(5.2K,2T) &= -\frac{\tilde{K}_{33}}{C_{33}}m_z^2 = 1.8 \times 10^{-6} \\ \frac{\Delta C_{33}}{C_{33}}(5.8K,8T) &= -\frac{4\tilde{K}_{33}^2\chi + 2\tilde{V}_{333}}{C_{33}}m_z^2 = -.002 \end{aligned} \tag{A7}$$

At zero field [Fig. 4(a)], the onset of the long-range linear antiferromagnetic ordering corresponds to a small slope variation in the data at T_{N_1}, while the elliptical magnetic ordering is easily identified by a pronounced anomaly at T_{N_2}. The comparison with the model predictions indicates that linear-quadratic coupling terms account for the discontinuous variation at the critical temperatures while biquadratic terms are necessary in order to qualitatively reproduce the temperature dependence observed at lower temperatures. Thus, the variation of C_{33} for $T < T_{N2}$ can be associated with that of $V_{331}S_\perp^2$ given by Eqs. (A7), while the coupling with S^2 is negligible

($V_{333} \simeq 0$). Furthermore, the discontinuous variation observed at both critical temperatures are used to set K_{33} and K_{31}. The remaining coefficient $\widetilde{V}_{333}$ and $\widetilde{K}_{33}$ are necessary in order to account for the field dependence. While $\widetilde{K}_{33}$ is determined independently according to magnetostriction measurements[37] along the c axis (e_{33}) using Eqs. (A7), $\widetilde{V}_{333}$ is adjusted to qualitatively reproduce the lower field dependence measured at $T = 5.8$ K [Fig. 4(c)].

*Corresponding author: gquirion@mun.ca

[1] M. F. Collins and O. A. Petrenko, Can J. Phys. **75**, 605 (1997).
[2] T. Kimura, Annu. Rev. Mater. Res. **37**, 387 (2007).
[3] M. L. Plumer, A. Caillé, and K. Hood, Phys. Rev. B **39**, 4489 (1989).
[4] M. L. Plumer, A. Caillé, A. Mailhot, and H. T. Diep, *Magnetic System with Competing Interaction* (World Scientific, Singapore, 1994).
[5] M. L. Plumer, K. Hood, and A. Caillé, Phys. Rev. Lett. **60**, 45 (1988).
[6] M. L. Plumer and A. Caillé, Phys. Rev. B **41**, 2543 (1990).
[7] H. T. Diep, ed., *Frustrated Spin Systems* (World Scientific, Singapore, 2004).
[8] M. L. Plumer and A. Caillé, Phys. Rev. B **37**, 7712 (1988).
[9] G. Quirion, T. Taylor, and M. Poirier, Phys. Rev. B **72**, 94403 (2005).
[10] M. Poirier, J. C. Lemyre, P.-O. Lahaie, L. Pinsard-Gaudart, and A. Revcolevschi, Phys. Rev. B **83**, 054418 (2011).
[11] H. Kawamura, J. Phys. Soc. Jpn. **56**, 474 (1987).
[12] H. Kawamura, J. Phys. Condens. Matter **10**, 4707 (1998).
[13] H. T. Diep, ed., *Magnetic Systems with Competing Interactions* (World Scientific, Singapore, 1994).
[14] H. Weber, D. Beckmann, J. Wosnitza, H. v. Löhneysen, and D. Visser, Int. J. Mod. Phys. B **9**, 1387 (1995).
[15] P.-É. Melchy and M. E. Zhitomirsky, Phys. Rev. B **80**, 064411 (2009).
[16] G. Quirion, X. Han, M. L. Plumer, and M. Poirier, Phys. Rev. Lett. **97**, 077202 (2006).
[17] P. Azaria, B. Delamotte, and T. Jolicoeur, Phys. Rev. Lett. **64**, 3175 (1990).
[18] M. L. Plumer and A. Mailhot, J. Phys. Condens. Matter **9**, L165 (1997).
[19] B. Delamotte, D. Mouhanna, and M. Tissier, Phys. Rev. B **69**, 134413 (2004).
[20] A. Peles, B. W. Southern, B. Delamotte, D. Mouhanna, and M. Tissier, Phys. Rev. B **69**, 220408(R) (2004).
[21] P. Calabrese, A. Pelissetto, and E. Vicari, Nucl. Phys. B **709**, 550 (2005).
[22] K. Kanki, D. Loison, and K. D. Schotte, J. Phys. Soc. Jpn. **75**, 015001 (2006).
[23] V. Thanh and H. T. Diep, J. Appl. Phys. **103**, 07C712 (2008).
[24] R. M. Morra, W. J. L. Buyers, R. L. Armstrong, and K. Hirakawa, Phys. Rev. B **38**, 543 (1988).
[25] H. A. Katori, Y. Ajiro, T. Asano, and T. Goto, J. Phys. Soc. Jpn. **64**, 3038 (1995).
[26] T. Asano, Y. Ajiro, M. Mekata, K. Kamishima, K. Koui, T. Goto, M. Furusawa, and H. Hori, J. Phys. Soc. Jpn. **66**, 460 (1997).
[27] P. B. Johnson, J. A. Rayne, and S. A. Friedberg, J. Appl. Phys. **50**, 1853 (1979).
[28] Y. Trudeau, M. L. Plumer, M. Poirier, and A. Caillé, Phys. Rev. B **48**, 12805 (1993).
[29] D. Beckmann, J. Wosnitza, H. v. Löhneysen, and D. Visser, Phys. Rev. Lett. **71**, 2829 (1993).
[30] X. Zhu and M. B. Walker, Phys. Rev. B **36**, 3830 (1987).
[31] W. Rehwald, Adv. Phys. **22**, 721 (1973).
[32] E. K. H. Salje, Acta Crystallogr. Sec. A **47**, 453 (1991).
[33] E. K. H. Salje, B. Wruck, and H. Thomas, Z. Phys. B **82**, 399 (1991).
[34] G. Quirion, W. Wu, O. Aktas, J. Rideout, M. J. Clouter, and B. Mróz, J. Phys. Condens. Matter **21**, 455901 (2009).
[35] G. Quirion, F. S. Razavi, B. Dumoulin, M. Poirier, A. Revcolevschi, and G. Dhalenne, Phys. Rev. B **58**, 882 (1998).
[36] Y. Trudeau, M. Poirier, and A. Caillé, Phys. Rev. B **46**, 169 (1992).
[37] J. A. Rayne, J. G. Collins, and G. K. White, J. Appl. Phys. **55**, 2404 (1984).
[38] B. Wolf, S. Schmidt, H. Schwenk, S. Zherlitsyn, and B. Lüthi, J. Appl. Phys. **87**, 7055 (2000).
[39] J. A. Rayne, J. G. Collins, and G. K. White, J. Appl. Phys. **52**, 1977 (1981).
[40] G. Quirion, M. J. Tagore, M. L. Plumer, and O. A. Petrenko, Phys. Rev. B **77**, 094111 (2008).
[41] G. Quirion, M. J. Tagore, M. L. Plumer, and O. A. Petrenko, J. Phys. Conf. Ser. **145**, 012070 (2009).
[42] G. Quirion, M. L. Plumer, O. A. Petrenko, G. Balakrishnan, and C. Proust, Phys. Rev. B **80**, 064420 (2009).
[43] N. Achiwa, J. Phys. Soc. Jpn. **27**, 561 (1969).